Energy Advances

ROYAL SOCIETY OF CHEMISTRY

PAPER

View Article Online
View Journal

Cite this: DOI: 10.1039/d5ya00313j

Highly active Cu-freudenbergite/TiO_2 heterojunction for solar-driven hydrogen evolution and 5-hydroxymethylfurfural oxidation

Panagiotis Tzevelekidis,[a] Elias Sakellis,[bc] Loukas Koutsokeras,[c] Olga Martzoukou,[d] Nikos Boukos[b] and Christiana A. Mitsopoulou *[a]

The pursuit of efficient photocatalytic systems for solar light-driven hydrogen evolution (HER) drives the search for novel semiconductor materials capable of forming advanced heterojunctions. Herein, we report the first synthesis of a non-stoichiometric, Cu-substituted freudenbergite (Cu-FDT) *via* a facile co-precipitation method. Comprehensive characterization (PXRD, XPS, RAMAN, HR-TEM/STEM-EDS) confirms the formation of a phase-pure freudenbergite structure with nanoplatelet morphology and mixed-valent Ti^{4+}/Ti^{3+}. Electronic characterization (UV-DRS, Mott–Schottky) reveals a bandgap (E_g) value of 2.95 eV enabling extended solar light harvesting and a band alignment perfectly suited for HER, coupled with a strong oxidation potential for the valence band (VB). A modified synthetic approach, involving the addition of water during Cu-FDT peptization, enabled the *in situ* fabrication of a Cu-FDT/TiO_2 heterojunction. The TiO_2 phase (anatase, mixed phase, rutile) was tuned by varying the calcination temperature. Photocatalytic performance toward HER was evaluated for all composites to elucidate the effect of excess surface Na^+ on photocatalytic activity. The optimal catalyst, a 1 wt% Pt-loaded, desodiated Cu-FDT/anatase heterojunction (1 wt% Pt@Cu-FDT_A deNa), achieved a high hydrogen production rate of 7183 μmol g^{-1} h^{-1} under solar irradiation. To correlate electrochemical properties with HER performance, EIS, photocurrent density, and LSV measurements toward the HER were conducted on anatase TiO_2, Cu-FDT and their heterojunction, comparing Na^+-rich and desodiated surfaces. Mott–Schottky analysis confirmed a direct Z-scheme charge transfer mechanism, enabling superior charge separation while preserving strong redox potentials. Furthermore, the high oxidative power of the heterojunction was further demonstrated by the near-complete mineralization of 5-hydroxymethyl furfural (5-HMF), with only minimal yields of partial oxidation products 5-hydroxymethyl-2-furancarboxylic acid (HMFCA) and 2,5-diformylfuran (DFF). These findings highlight the potential of this novel photocatalyst to simultaneously drive HER and challenging oxidation reactions, thus coupling renewable H_2 evolution with the potent oxidative power of photogenerated holes (h^+) in the VB of Cu-FDT.

Received 29th October 2025,
Accepted 4th January 2026

DOI: 10.1039/d5ya00313j

rsc.li/energy-advances

1. Introduction

Depletion of fossil fuels and the resulting impact on Earth's climate and the global economy have shifted the attention to the pursuit of renewable energy sources with zero carbon emissions.[1] Solar-driven photocatalysis and especially water splitting into H_2 and O_2, represents a promising pathway for sustainable energy conversion as H_2 energy content far surpasses the energy obtained from the combustion of fossil fuels.[2] However, major drawbacks of this process include the low utilization of the full potential of photocatalysts due to rapid electron (e^-)–hole(h^+) recombination and the sluggish reaction kinetics of the oxygen evolution reaction (OER).[3] Titanium dioxide (TiO_2) has been widely studied as a benchmark photocatalyst due to its robust stability, low cost, and favorable band positions for both the hydrogen evolution reaction (HER) and the OER. Nevertheless, certain limitations such as the large band gap (3.2 eV) of anatase – the most photocatalytic active phase of TiO_2 – which in turn restricts its use in the UV region, as well as the inherent fast charge recombination, hinder practical application.[4,5]

[a] *Inorganic Chemistry Laboratory, Department of Chemistry, National and Kapodistrian University of Athens, 15771 Zografou, Greece. E-mail: cmitsop@chem.uoa.gr*
[b] *Institute of Nanoscience and Nanotechnology, National Centre of Scientific Research "Demokritos", Agia Paraskevi, 15341, Greece*
[c] *Section of Condensed Matter Physics, Department of Physics, National and Kapodistrian University of Athens, Athens, 15784, Greece*
[d] *Enzyme and Microbial Biotechnology Unit, Department of Biology, National and Kapodistrian University of Athens, Athens, 15784, Greece*

Several approaches have been employed to overcome the limitations of TiO_2, including doping with transition metals (*e.g.*, Fe, Cu, Ni) to create mid-gap states and extend the light absorption into the visible-light region, as well as anionic doping (*e.g.*, N, S).[6–10] Furthermore, decoration with noble metal nanoparticles (*e.g.*, Au, Ag, Pd) has been employed to exploit the surface plasmon resonance (SPR) effect, which enhances light harvesting and promotes charge separation.[6,11] Another well-established strategy is the addition of co-catalysts such as Cu and Pt for HER, since they serve as electron sinks, that efficiently collect photogenerated electrons from the TiO_2 light-harvesting support and facilitating the reduction of protons (H^+) to H_2.[12–14]

Constructing heterojunctions between TiO_2 and other semiconductors is an effective alternative strategy, proven to enhance charge separation through Type II, Z- and S-scheme charge transfer. Many semiconductors have been used in heterojunctions with anatase TiO_2, such as g-C_3N_4, CdS, $ZnIn_2S_4$, and others, known for creating efficient heterojunctions and exhibiting notable activities for H_2 generation under solar-light irradiation.[15–17] In this context, the combination of TiO_2 with other TiO_2 polymorphs like rutile, brookite and TiO_2(B) and perovskites has emerged as a powerful strategy for developing efficient heterojunction systems, as strong interfacial bonding and optimal band alignment with anatase significantly enhances charge separation.[18–21] Recent work on Cu- and Ni-doped $Na_2Ti_6O_{13}$ and $Na_2Ti_3O_7$ has shown that transition-metal incorporation can tune the band structure and electrical conductivity of tunnel titanates, suggesting a viable route toward visible-light-responsive, mixed-valence Ti^{3+} systems.[22–24]

Freudenbergite, $Na_2Fe^{3+}{}_2Ti_6O_{16}$, is a less-explored titanium-based material that offers a compelling partner for forming such heterojunctions. First identified by Frenzel in 1958 and later structurally characterized by Ishiguro *et al.* in 1978, it exhibits a titanate-like structure and a monoclinic space group (*C*2/*m*) consisting of TiO_6 octahedra forming tunnels that accommodate charge balancing cations like Na^+.[25,26] Notably, this structure allows substantial cationic substitution with transition metals on the Ti^{4+} sites, which significantly narrows the bandgap and enhances visible-light absorption.[27,28] Recent reports on Na–Mg–Fe–Ti–O solid solutions confirm the compositional flexibility and photoactive potential of these freudenbergite-type lattices[29,30] Ciocarlan *et al.* reported a heterojunction of freudenbergite with Zn–Ni ferrite which demonstrated exceptional efficiency in organic dye degradation (methylene blue and rhodamine G) under visible-light irradiation owing to the small band gap of ferrite and $FeNaTi_3O_8$ freudenbergite ($\sim$2.2 eV), as well as due to the strong adsorption properties of $FeNaTi_3O_8$.[31] The electronic properties of transition metal-substituted freudenbergites make them particularly attractive for photocatalytic applications as the band structure of $FeNaTi_3O_8$ creates a sufficiently positive valence band (VB) position for strong oxidative activity while maintaining a sufficient reductive conduction band (CB) for H_2O reduction, while the presence of mixed valence states (Ti^{4+}/Ti^{3+} and $Fe^{3+/2+}$) further enhances carrier dynamics.[31–33]

Despite these promising findings, no study has yet reported the substitution of Fe by Cu within the freudenbergite lattice, nor the coexistence of Ti^{3+} species stabilized through this substitution. Such substitution is expected to include unique electronic perturbations due to the redox flexibility of Cu^{2+}/Cu^{1+} and its strong interaction with Ti^{3+} sites, which may synergistically enhance charge-transfer and improve photocatalytic activity.

The implementation of efficient overall water splitting systems remains a formidable challenge, primarily due to the thermodynamically demanding OER. To overcome this bottleneck, a common strategy employs sacrificial electron donors such as triethanolamine (TEOA) or methanol (MeOH), which act as h^+ scavengers. The rapid consumption of h^+ supresses e^-–h^+ recombination, thereby increasing the lifetime of e^- available for HER.[34] In this context, the photocatalytic oxidation and reforming of biomass-derived substrates has emerged as a promising alternative strategy.[35] 5-Hydroxymethylfurfural (5-HMF) is a pivotal, biomass-derived platform molecule that serves as a versatile precursor for a wide range of valuable chemicals. Its structure comprises a furan ring with aldehyde and hydroxymethyl functional groups that allow for selective oxidation into high-value products, such as 2,5-furandicarboxylic acid (FDCA), 2,5-diformylfuran (DFF) and 5-hydroxymethyl-2-furancarboxylic acid (HMFCA).[36] The photocatalytic oxidation of 5-HMF offers a sustainable approach to replace classic electron donors and recent studies have demonstrated the photocatalytic selective conversion of 5-HMF to value added chemicals coupled with H_2 generation using heterojunctions of semiconductor materials such as g-C_3N_4, TiO_2, In_2O_3 and $ZnIn_2S_4$.[37–39]

Herein, to the best of our knowledge, we report for the first time the synthesis of a Cu-substituted freudenbergite (Cu-FDT), *via* a facile co-precipitation route, leading to the stabilization of mixed-valence Ti^{3+}/Ti^{4+}–Cu^{2+} sites. The resulting material was comprehensively characterized: its structure and morphology were elucidated by PXRD, XPS, Raman, HR-TEM and STEM-EDS, while its electronic properties were determined using UV-DRS and Mott–Schottky analysis. Notably, we discovered that introducing a minimal quantity of water during Cu-FDT synthesis facilitated the *in situ* formation of a heterojunction between Cu-FDT and anatase TiO_2. This *in situ* formation is a key advantage for heterojunction formation, ensuring optima interfacial contact. The phase composition and stability of this composite were further examined, revealing that the TiO_2 polymorph and Cu-FDT content could be precisely tuned by varying the calcination temperature. The photocatalytic performance of these heterojunctions was evaluated for solar driven HER before and after the removal of excess surface sodium. The most active catalyst-namely, the 1 wt% Pt-loaded, desodiated CuFDT/anatase heterojunction (1 wt% Pt@Cu-FDT$_A$ deNa), exhibited outstanding performance, achieving a remarkable HER activity of 7183 $\mu molH_2\ g^{-1}\ h^{-1}$ using TEOA as a sacrificial electron donor. Electrochemical measurements (EIS, photocurrent density, LSV) confirmed enhanced activity for HER in both Na^+-rich and desodiated Cu-FDT/anatase heterojunctions. The superior photocatalytic performance of the

desodiated photocatalysts is attributed primarily to improved surface properties that favor Pt co-catalyst loading and H_2O reduction. Mott–Schottky analysis of the optimal composite revealed the formation of a heterojunction with Fermi-band position pointing to a direct Z-scheme charge transfer mechanism at the Cu-FDT/anatase interface, which accounts for the superior spatial separation of photogenerated charge carriers while preserving the strong redox potential necessary to drive catalytic reactions. Finally, we demonstrated the practical oxidative capability of the heterojunction through the photocatalytic oxidation of the biomass-derived platform chemical, 5-HMF. The reaction pathway proceeded predominantly *via* deep oxidation of 5-HMF with only limited quantities of partial oxidation intermediates, HMFCA and DFF, being detected. This observation underscores the potent oxidative power of photogenerated h^+ residing in the VB of Cu-FDT, which drives the photooxidation of 5-HMF.

2. Experimental section

2.1 Materials

Titanium(IV) i-propoxide TTIP (97%), absolute ethanol – EtOH (99.8%), methanol – MeOH (99%), acetone – AcON (99%), copper(II) nitrate trihydrate – $Cu(NO_3)_2{\cdot}3H_2O$ (99%), anhydrous acetic acid – AA (99.8%), acetonitrile – MeCN, (99%) sodium hydroxide – NaOH pellets, HCl (37%) and triethanolamine – TEOA (98%) were purchased from Acros Organics and used without further purification. 5-Hydroxymethyl furfural – 5-HMF (98%) was purchased from Sigma-Aldrich. Barium sulfate – $BaSO_4$ (99%) and potassium tetrachloro-platinate – K_2PtCl_4 were obtained from Thermo Fisher Scientific. Nafion was obtained from Sigma-Aldrich. A Rephile Milli-Q system provided Ultra-pure water (MilliQ H_2O) which was used for all the synthetic and experimental procedures. Argon – Ar (99%), nitrogen – N_2 (99.7%) gasses and compressed air were supplied by Revival N.C.

2.2 Photocatalyst preparation

2.2.1 Cu-freudenbergite (Cu-FDT). Cu-FDT was synthesized *via* a co-precipitation method. Specifically, 1.53 ml (0.005 mol) TTIP was added dropwise, under continuous stirring to 10 ml of deaerated, Ar-saturated EtOH in a round bottom flask. Subsequently, 0.48 ml (0.008 mol) of AA were added to initiate hydrolysis and coordination with Ti(IV). The solution was stirred for 1 h in the dark and at 25 °C, after which a 3 mol% $Cu^{(2+)}$ equivalent (relative to $Ti^{(4+)}$) was added in the form of $Cu(NO_3)_2{\cdot}3H_2O$ dissolved in 1 ml EtOH. The resulting homogenous light blue solution was kept in the dark under constant stirring for an additional 1 hour. Next, 4 ml of a 2 M NaOH solution (Na/Ti molar ratio = 1.6) was rapidly injected causing the mixture to immediately turn opaque. Over the following hour the dispersion transformed into a light blue, highly viscous gel. The gel was subjected to ultrasonication for 1 h in 5 ml AcON and after vacuum drying, the obtained powder was washed repeatedly with ethanol to remove unreacted precursors and then calcined at 550 °C for 4 h (heating rate: 10 °C min^{-1}) to yield the final product. Pure TiO_2 anatase was synthesized following the same experimental procedure, without the addition of Cu precursor and used for the Mott–Schottky experiments.

2.2.2 Cu-FDT/TiO_2 heterojunction. Heterojunctions of Cu-FDT with different TiO_2 were synthesized *in situ* following the same synthetic procedure, but with an additional step of introducing minimal amount of MilliQ H_2O before the introduction of NaOH. Specifically, to the mixture of TTIP, $Cu(NO_3)_2{\cdot}3H_2O$ and AA in the ratios mentioned in Section 2.2.1, 100 μl of H_2O were added, causing the solution to turn colourless but without any precipitation being observed. The rest of the synthetic procedure remained the same and the resulting powder obtained after vacuum drying was washed repeatedly with ethanol and water and calcined at 550 °C (4 h), 650 °C (4 h), 750 °C (4 h), and 850 °C (4 h). The final samples were finely ground and denoted as Cu-FDT_A, Cu-FDT_B, Cu-FDT_C, Cu-FDT_D.

2.2.3 Desodiation of the photocatalysts. Another set of catalysts was prepared by removing excess Na^+ ions from the catalytic surface. Following the synthetic and cleaning procedures in Section 2.2.2, the photocatalyst powders were dispersed in 200 ml of a 1 M HCl solution at a concentration of 1 mg ml^{-1} and subjected to ultrasound treatment for 2 h to ensure thorough desodiation. Subsequently, the photocatalysts underwent rigorous washing with MilliQ H_2O to eliminate residual NaCl, until the pH of the supernatant reached 6.8–7. The desodiated powders were then subjected to calcination under the same conditions as previously described in Section 2.2.2. The resulting photocatalysts, calcined at 550 °C (4 h), 650 °C (4 h), 750 °C (4 h), and 850 °C (4 h) were denoted as Cu-FDT_A deNa, Cu-FDT_B deNa, Cu-FDT_C deNa, Cu-FDT_D deNa.

2.2.4 Pt photodeposition. Photodeposition of the Pt co-catalyst for the hydrogen evolution reaction was conducted as follows: 20 mg of the photocatalyst were dispersed in a 50% (v/v) aqueous MeOH solution within a glass reactor. A stoichiometric amount of K_2PtCl_4 was added to achieve 1 wt% Pt loading. The suspension was saturated with Ar for 30 min, to ensure an O_2-free environment. Photodeposition was carried out under UV-visible irradiation ($\lambda > 300$ nm) using a 300 W Xe solar simulator (Quantum Design, LSH302) equipped with an AM 1.5G filter. After 2 h of irradiation, the Pt-loaded photocatalyst was recovered by centrifugation, thoroughly washed with MilliQ H_2O, and dried at 80 °C for 12 h.

2.3 Structural and optical characterization

Powder X-ray diffraction was carried out in a Bruker D8 Advance diffractometer, operated in Bragg–Brentano geometry, at 40 kV and 25 mA. The X-ray source was a Cu anode with $\lambda = 1.5418$ Å for the $K\alpha_1$. The diffraction patterns were recorded for 10–85 $2\theta^\circ$ with step size of 0.02° 2θ s^{-1} and step duration at 0.22 s. Crystal phase indexing, crystallinity evaluation and relative percentages of the crystalline phases at each sample were performed using Diffrac. EVA software. Rietveld refinement was performed utilizing Profex software. The average crystallite

size was calculated for the (020) crystal plane of Cu-FDT at 47.5° employing the Scherrer equation:

$$D = \frac{k\lambda}{\beta(2\theta)\cos\theta} \quad (1)$$

where D represents the crystallite size, k is the shape factor, λ refers to the wavelength of the X-rays, θ is the Bragg angle and β (2θ) corresponds to the line broadening at full width at half-maximum (FWHM) of the (411) diffraction. For the PXRD analysis of Cu-FDT, the diffraction pattern was recorded for 3–85 $2\theta^\circ$, with a step size of 0.03° 2θ s^{-1} and step duration of 5 s, to ensure high data quality for the Rietveld refinement.

Raman analysis of the synthesized photocatalysts was conducted on a dual-source micro-Raman inVia Qontor spectrometer from Renishaw with the use of the 785 nm Ar laser beamline.

The X-ray photoelectron spectroscopy (XPS) experiments were carried out in an ultra-high vacuum system (UHV) equipped with an X-Ray gun. Unmonochromatized MgKα line at 1253.6 eV and two analyzer pass energies of 15 eV (giving a full width at half maximum (FWHM) of 0.85 eV for the Ag $3d_{5/2}$ peak) and 40 eV were used. The XPS core level spectra were analyzed using a fitting routine, which can decompose each spectrum into individual mixed Gaussian–Lorentzian peaks after a Shirley background subtraction. Errors in our quantitative data are found in the range of ~10%, (peak areas) while the accuracy for BEs assignments is ~0.1 eV. The samples were in powder form and pressed onto In foil while the analyzed area was a rectangle of 7.0 × 15 mm^2.

FT-IR spectroscopy was conducted on a Shimadzu IRAffinity spectrometer bearing an ATR (attenuated total reflection) QATR10 single-reflection accessory. Spectra were recorded in the range of 400–4000 cm^{-1}.

UV-DRS absorbance and reflectance spectra were recorded on a Shimadzou UV-260 spectrophotometer bearing an integrating sphere attachment (ISR-2600Plus) with $BaSO_4$ employed as reference. Catalyst powder and $BaSO_4$ were mixed in a ratio of 1 : 10, finely ground to create a homogenous mixture, and thinly pressed on the sample holder. Reflectance data were transformed into Kubelka–Munk plots for the calculation of the indirect bandgap of the semiconductors by plotting $(F(R_\infty)h\nu)^{1/2}$ *versus* the photon energy. Extrapolation of the linear part below the direct transition to the *x*-axis intercept gave the value of the indirect bandgap.

PL spectra were acquired with a Horiba Jobin-Yvon iHR320 spectrofluorometer using an excitation wavelength of 310 nm for all measurements.

Transmission electron microscopy (TEM) and scanning transmission electron microscopy (STEM) was conducted using a Talos F200i field-emission scanning transmission electron microscope (Thermo Fisher Scientific, Waltham, MA), operating at an acceleration voltage of 200 kV and integrated with a Bruker 6T/100 windowless energy-dispersive X-ray spectroscopy (EDAX) system (Hamburg, Germany). Ethanolic dispersions of catalyst samples were deposited onto nickel TEM grids *via* drop-casting for imaging. Quantitative size analysis was performed by statistically evaluating approximately 80 distinct nanoparticles using ImageJ processing software.

SEM (scanning electron microscopy) images were collected with a Quanta Inspect Microscope from FEI operating at 15–25 keV.

2.4 Electrochemical measurements

Photoelectrochemical and electrochemical measurements were performed using a standard three-electrode configuration with a VersaSTAT 3 Potentiostat/Galvanostat (AMETEK, Inc., USA), controlled by VersaSTAT software for data acquisition and analysis. For transient photocurrent and electrochemical impedance (EIS) measurements, the working electrode was prepared by drop-casting a catalyst ink onto an FTO glass substrate (1 cm × 1 cm). The ink was prepared by dispersing 5 mg of powder in 1 ml of 20% v/v Nafion ethanolic solution, followed by ultrasonication for 30 minutes and overnight drying at 60 °C. A Pt wire and an Ag/AgCl (saturated KCl) electrode served as the counter and reference electrodes, respectively, with a 0.2 M Na_2SO_4 aqueous solution as the electrolyte. Photocurrent density *versus* time (*I*–*t*) curves were recorded using chronoamperometry at a constant bias of 0.5 V *vs.* Ag/AgCl under chopped illumination from a 300 W Xe lamp, using light on/off cycles of 20 seconds each. EIS was conducted at the open-cirquit potential at the frequency range of 10 kHz to 0.01 Hz with an AC amplitude of 5 mV. For linear sweep voltammetry (LSV) measurements related to HER activity, the working electrode was prepared similarly by drop-casting the same catalyst ink onto a 1 cm × 1 cm carbon paper substrate. The 0.5 M H_2SO_4 solution which served as the electrolyte for HER was thoroughly deaerated for 30 min with Ar flow. LSV was carried out with a scan rate of 5 mV s^{-1}, and all polarization curves were *iR* corrected. The measured potentials were calibrated to the reversible hydrogen electrode (RHE) scale using the following relation:

$$E_{vs.\mathrm{RHE}} = E_{vs.\mathrm{Ag/AgCl}} + 0.059 \times \mathrm{pH} + 0.197\ \mathrm{V} \quad (2)$$

The Tafel slope was subsequently derived from the linear region of the corresponding Tafel plot. For the Mott–Schottky analysis, the working electrode was prepared by dispersing 5 mg of the photocatalyst in 50 µl of a 20% v/v Nafion solution in EtOH, followed by 5 min of ultrasonication to ensure homogeneity. The resulting ink was drop-cast onto a polished glassy carbon electrode (0.071 cm^2 surface area) and dried overnight at RT. Measurements were using the same counter and reference electrodes, and a 2 M KCl aqueous electrolyte solution. The Mott–Schottky plots were obtained at 1000 and 5000 Hz with a DC potential sweep from 0.3 to −1 V, under dark conditions, to assess the flat-band potential of the semiconductor photocatalyst.

For the determination of the relative band edge positions of Cu-FDT and TiO_2 anatase heterojunction components, a combined UV-DRS and Mott–Schottky analysis was employed. The flat-band potential obtained from Mott–Schottky measurements were used to approximate the CB edge positions of the

n-type semiconductors, while the VB positions were subsequently derived from UV-DRS according to the following relation:

$$E_{VB} = E_{CB} + E_g \quad (3)$$

where E_{VB} and E_{CB} represent the VB and CB edge positions respectively, and E_g is the bandgap energy obtained from Tauc plots.

2.5 Solar-driven photocatalytic H_2 evolution

Photocatalytic experiments under simulated solar light irradiation were conducted by dispersing 0.2 g L^{-1} of each photocatalyst in 10 ml of aqueous solution containing 10% (v/v) sacrificial donor (TEOA, MeOH, 5-HMF). The suspension was degassed and saturated with Ar under constant stirring before illumination. Next, the reactor was placed 25 cm away from a 300 W Xe lamp (as described in Section 2.2.4), which provided solar irradiation at wavelengths $\lambda > 300$ nm for 6 h. At each time interval (1 h), 50 µl of gas was sampled from the headspace of the gastight reactor and injected into the gas chromatograph (GC). The GC was a Chromatec Crystal 9000 equipped with a TCD detector, operated at 70 °C and 150 °C, oven and detector temperature, respectively. Separation was achieved using a 5 Å molecular sieve column, with N_2 as the carrier gas. Data acquisition and quantification were performed using the Chromatec (Analytic) software, and GC calibration was performed as described in previously published protocols.[40]

2.6 Photooxidation of 5-(hydroxymethyl) furfural (5-HMF)

The conversion of the platform chemical 5-HMF was investigated as a sacrificial electron donor in aqueous solutions, for H_2 evolution under solar light irradiation, targeting a sustainable process for oxidative production of value-added chemicals such as 2,5-furandicarboxylic acid (FDCA) and 2,5-diformylfuran (DFF) coupled with HER. Photocatalytic experiments were conducted using 2–4 mg of catalyst dispersed in 10 ml of either aqueous, MeCN or an 80 : 20 MeCN : H_2O mixed solvent dispersion, under Ar saturated conditions, unless otherwise stated. The first set of experiments employed 0.2 g L^{-1} catalyst concentration, a 10 mM 5-HMF solution in MilliQ H_2O and 12 h of Xe lamp irradiation (as described in Section 2.2.4). The second set used the same 5-HMF concentration (10 mM) with 0.4 g L^{-1} catalyst dosage and shorter irradiation time (6 h) to identify the dominant active species responsible for 5-HMF oxidation. H_2 gas evolved during the reaction was collected from the reactor head space and quantified *via* GC as in Section 2.5. Liquid-phase products were analysed by HPLC and UV-Vis after removal of the photocatalyst *via* filtration and appropriate dilution. HPLC analysis was performed on an Agilent HPLC 1220 Infinity LC System using a C_{18} reversed-phase column (Poroshell 120 EC-C18, 4 µm, 4.6 by 150 mm; Agilent). The elution profile (0.75 ml min^{-1}) consisted of a 10-min isocratic elution, and the mobile phase was a 20% (v/v) MeOH solution. Excitation wavelengths of the detector were set at 230 and 270 nm. The photooxidation of 5-HMF was quantified by UV-Vis spectroscopy (U-2000 (Hitachi, Berkshire, United Kingdom)), monitoring the characteristic absorbance at 284 nm in H_2O and at 280 nm in MeCN 80% mixtures. Control experiments with 10 mM 5-HMF in H_2O and MeCN 80% for 12 h and 6 h light duration experiments without catalyst and under Ar atmosphere, were conducted for comparison and revealed negligible photolysis of 5-HMF. The samples used for HPLC and UV-Vis spectroscopy were diluted to 50 µM and 200 µM respectively, based on the concentration of 5-HMF before light irradiation.

3. Results and discussion

3.1 Structural and morphological characterization

The successful synthesis of copper-substituted freudenbergite (Cu-FDT) was confirmed through Rietveld refinement of powder X-ray diffraction (PXRD) data. The experimental pattern of the synthesized material matched the reference pattern for stoichiometric freudenbergite ($FeNaTi_3O_8$, COD No. 9011187), which crystallizes in the monoclinic C12/m1 space group. Refinement indicates that Cu^{2+} ions substitute for Fe^{3+} within the freudenbergite tunnel structure (Fig. 1a and Fig. S1, Table S1). Charge balance is likely maintained by the coexistence of Ti^{3+} and Ti^{4+}. The most intense diffractions were observed at 2θ = 10.1°, 11.1°, 23.8°, 24.4°, 28.7°, 29.7°, 44.3°, 47.7°, and 67.1° and were indexed to the (001), (200), (110), (002), (111), (310), (003), (020), and (023) lattice planes, respectively. A minor, unidentified impurity phase (<1 wt%) was detected but considered negligible for the structural analysis. Notably, the addition of a Cu^{2+} precursor was essential for the crystallization of the freudenbergite phase. Reaction mixtures without the Cu^{2+} precursor resulted exclusively in the crystallization of anatase TiO_2, which was used for comparison. The Cu-FDT material was found to exhibit an average crystallite size of 22.4 ± 0.2 nm measured on the (020) direction (Table S3). Data quality made the calculation of microstrain due to substitution of Fe^{3+} with Cu^{2+} and the contribution from the existence of oxygen defects near Ti^{3+} positions not possible. Nonetheless, differences in the intensity of certain diffractions between calculated and the experimental pattern indicate subtle changes in bond length due to Cu^{2+} incorporation (Fig. S1). More specifically, the refined lattice parameters were determined to be a = 1.2245(1) nm, b = 0.38209(4) nm, c = 0.64920(8) nm and β = 107.68° (Table S1). A comparative analysis with the pristine lattice parameters of the referenced.-cif file reveals a discernible shift from the pristine Fe^{3+} bearing freudenbergite ($FeNaTi_3O_8$). The observed anisotropic changes in the unit cell and especially the contraction of the a and b parameters, Δa = −0.0022 nm and Δb = −0.0002 nm respectively, as well as the expansion along the c axis and the significant increase in the β angle, Δc = 0.0009 and $\Delta\beta$ = 0.52°, are attributed to the successful incorporation of Cu^{2+} in the crystal structure.[25] This distorted pattern is characteristic of the Jahn–Teller effect, a well-known phenomenon of d^9 cations like Cu^{2+}. This effect causes a cooperative elongation of the $(Cu/Ti)O_6$ octahedra, while the substitution of Fe^{3+} (0.065 nm) by the larger Cu^{2+} (0.073 nm) ion is the primary reason for the

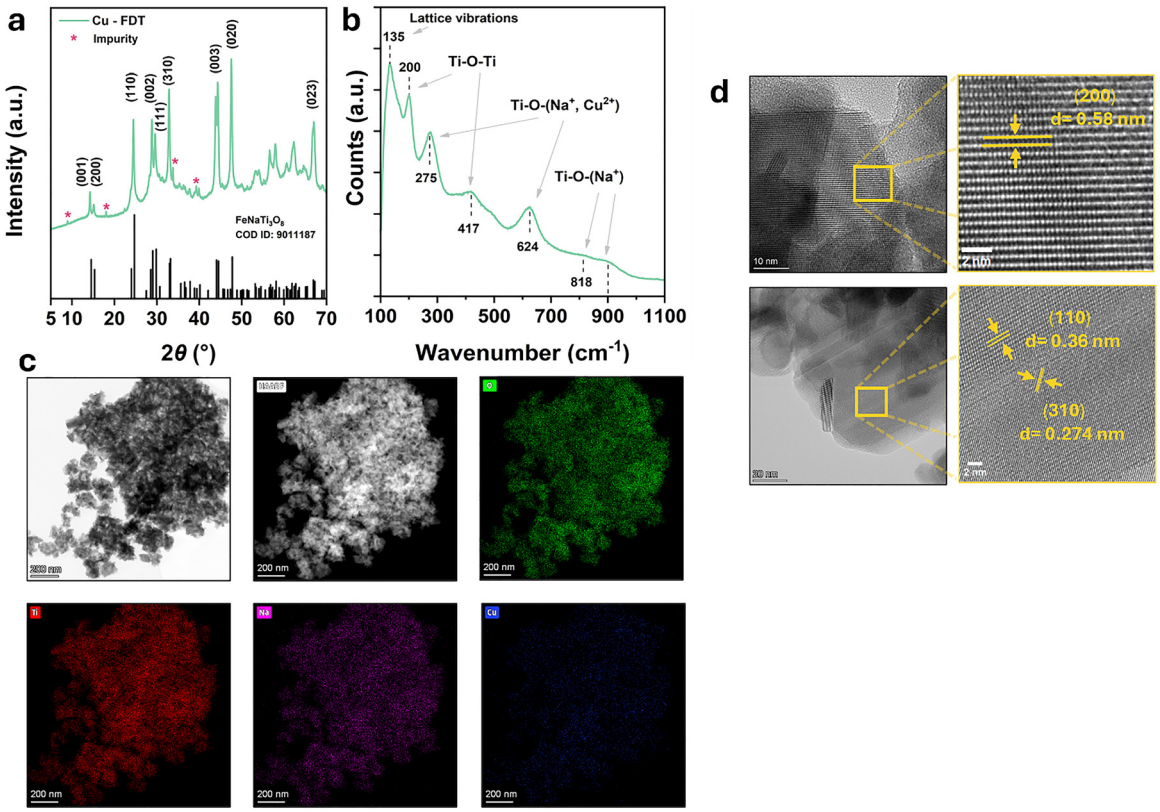

Fig. 1 (a) PXRD pattern of Cu-FDT and of freudenbergite presented for reference, (b) Raman spectra of the synthesized material, (c) STEM and elemental maps of O, Ti, Na and Cu, (d) HR-TEM images and *d*-spacing of the selected areas.

observed structural changes. Regarding charge neutrality of the crystal lattice, the incorporation of divalent copper in a structure typically balanced by trivalent cations indicates a charge compensation mechanism. The observed expansion along the *c* axis is consistent with the co-existence of a larger cation in the octahedral sites. This suggests that a portion of Ti^{4+} (0.605 nm) is reduced to Ti^{3+} (0.67 nm) to maintain neutrality in the new crystal lattice. The combined effects of the Jahn–Teller effect induced by Cu^{2+} and the possible presence of Ti^{3+} could explain the calculated differences in the crystal lattice of Cu-FDT in comparison to the known structure of freudenbergite.[41,42]

Raman spectroscopy provided further understanding into the bonding environment of the Cu-FDT unit cell (Fig. 1b). The framework of the freudenbergite, being structurally analogous to titanate nanotubes, contains edge- and corner-sharing TiO_6 octahedra. This similarity results in vibrational spectra varying significantly from the more densely packed frameworks of well-known TiO_2 polymorphs like anatase and rutile. Here, the spectrum is defined by bands at 135 cm^{-1}, associated with lattice vibrations at 200 and 417 cm^{-1} assigned to Ti–O–Ti bending and stretching vibrations.[43] The features at 275 and 624 cm^{-1} are associated with metal-oxygen bonds (Ti–O–Na^+ or Cu^{2+}).[44] Furthermore, the higher-frequence bands at 818 and 900 cm^{-1} are indicative of Ti–O–Na stretching modes. The red-shifting of the band at 624 cm^{-1} as compared to Fe^{3+}-containing freudenbergite implies the existence of Cu^{2+} and is directly correlated to bond elongation due to the Jahn–Teller effect induced by the latter.[43,44]

Elemental mapping *via* STEM-EDS confirmed the homogenous distribution of oxygen (O), titanium (Ti), sodium (Na) and copper (Cu) throughout the surface of the new material, indicating a uniform elemental composition (Fig. 1c). Quantitative analysis of the EDS spectra yielded an overall elemental stoichiometry distinct from $CuNaTi_3O_8$, primarily due to significantly higher sodium content (Table S2). Excess sodium can be explained by residual Na^+ ions on the surface of the material contributing to the amorphous part of the sample rather than the unit cell of Cu-FDT.

HR-TEM images of the synthesized photocatalyst confirmed interplanar crystal spacings of 0.58 nm, 0.36 nm and 0.274 nm assigned to (200), (110) and (310) facets of the freudenbergite unit cell respectively (Fig. 2d and Fig. S2c). The synthesized material exhibited predominantly a nanoplatelet-like morphology and heavy aggregation, a phenomenon arising from the co-precipitation and dehydration steps comprising the synthetic procedure. Image analysis revealed a polydisperse size distribution with an average size at 23.3 nm with most of the particles measuring less than 50 nm (Fig. S2a and b).

The XPS survey spectra for Cu-FDT confirmed the presence and oxidation states of Ti, Cu, O and Na which comprise the unit cell of Cu-FDT (Fig. S3a). Determination of Ti valences present is pivotal for understanding the mechanism behind the

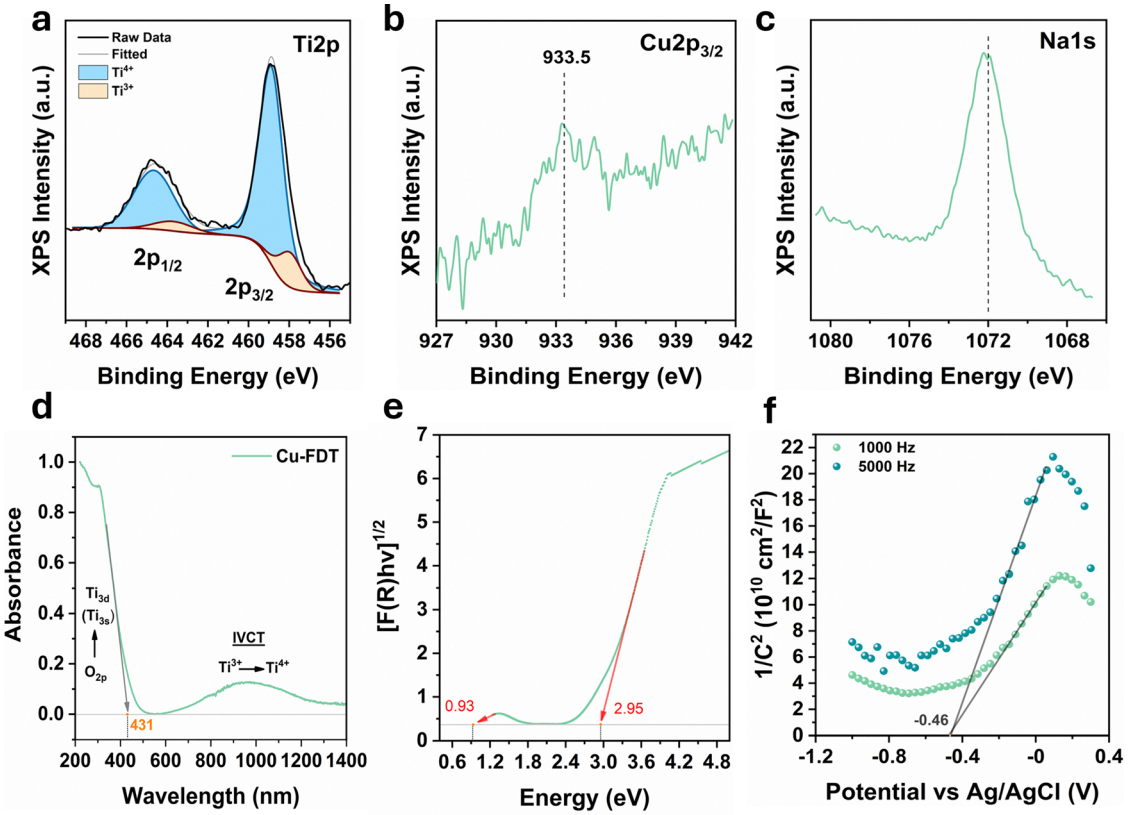

Fig. 2 (a)–(c) Fitted XPS spectra of the Ti 2p core level (a), Cu $2p_{3/2}$ core level (b), and Na 1s core level (c) and (d) UV-DRS absorbance spectra of Cu-FDT photocatalyst, (e) Tauc plot constructed from the Kubelka–Munk transformation of Cu-FDT reflectance spectra, (f) Mott-Schottky plots obtained at 1000 and 5000 Hz.

charge balancing in the unit-cell of the synthesized material. The replacement of Fe^{3+} with Cu^{2+} necessitates such a mechanism through the partial reduction of Ti^{4+} to Ti^{3+} and possibly the co-existence of O vacancies near the Ti^{3+} ions. High resolution analysis of the Ti 2p core level revealed a doublet with spin–orbit splitting of 5.75 eV. The spectrum was characterized by a primary doublet with the Ti $2p_{3/2}$ peak at 459 ± 0.1 eV, assigned to Ti^{4+} in the TiO_6 octahedra of a TiO_2-like environment. Critically, a second doublet was identified at a lower binding energy (Ti $2p_{3/2}$ at 458 ± 0.1 eV), which was attributed to the presence of Ti^{3+} species.[45] Ti^{3+} contribution was calculated to be 12.5% for the total amount of Ti present in the sample (Table S3). The Cu $2p_{3/2}$ spectra main feature, located at 933.5 eV indicated the presence of copper in the 2^+ state (Fig. 2b) while the Na 1s spectrum at 1072 eV was consistent with Na-Ti-O bonding (Fig. 2c).[46–48] The C 1s peak was deconvoluted into three components corresponding to C–C/C–H, C–O, and O–C=O bonds (Fig. S3b) indicating the presence of residual acetates on the surface of Cu-FDT as a consequence of the use of acetic acid and acetone during synthesis.[49]

3.2 Optical and electrochemical characterization

Optical characterization *via* UV-DRS provided critical insights into the electronic properties and band structure of the synthesized Cu-FDT material. The Tauc plot derived from the transformed reflectance spectrum revealed an indirect E_g value of 2.95 eV (Fig. 2e), corresponding to an absorption edge at 431 nm (Fig. 2d). The bandgap transition, based on the unit-cell configuration, involved the excitation of an electron from the O 2p orbital-consisting valence band (VB) to the conduction band (CB) comprised of hybridized states from Ti^{3+}/Ti^{4+} and Cu^{2+}. Furthermore, a distinct low-energy absorption band was observed at approximately 965 nm (0.93 eV) (Fig. 2d and e). This band lied at considerably longer wavelengths than typical Cu^{2+} d–d transitions that could potentially be immobilized on the semiconductor's surface and exhibited characteristics consistent with an intervalence charge transfer (IVCT) process.[50] The broad, asymmetric shape and energy of this transition suggests electron transfer between adjacent mixed-valence sites, most likely between Ti^{3+} and Ti^{4+} centres or from Cu^{2+} to Ti^{4+}. This IVCT band provided strong evidence of electronic coupling between metal centres in the mixed-valence Cu-FDT crystal system, further confirming the successful integration of Cu into the titanate framework and the creation of new electronic states within the bandgap.[50,51]

To elucidate the electronic band structure and thermodynamic potentials of the Cu-FDT photocatalyst, electrochemical characterization was conducted. Mott–Schottky plots were constructed and the negative slope obtained revealed that Cu-FDT is a n-type semiconductor.[52] As a result the flat-band potential was used to approximate the conduction band edge position, as for n-type semiconductors the flat-band potential is

known to lie close to the CB (Fig. 2f).[53] The energy of the CB minimum defined the thermodynamic driving force of the photoexcited electrons to participate in reduction reactions, such as HER. Two different frequencies (100 and 5000 Hz) were used to ensure reproducibility, and the flat-band potential was calculated to be −0.46 V *vs.* Ag/AgCl. Conversion to NHE (pH = 7) was performed using formula (2) and the CB of Cu-FDT was determined to be at −0.25 V *vs.* NHE using eqn (2).[54]

By correlating the bandgap energy value obtained from the Tauc plot with the experimentally determined conduction band potential, the valence band maximum of Cu-FDT was identified as +2.7 V *vs.* NHE employing relation (3). This electronic structure positions Cu-FDT as a highly promising material for both photocatalytic oxidation processes and HER, as it provides strong oxidative VB and sufficiently reductive CB.[4]

3.3 Fabrication of Cu-FDT/TiO_2 heterojunctions and surface Na^+ effect on the heterojunction formation

The intentional *in situ* construction of a heterojunction between copper substituted freudenbergite (Cu-FDT) and TiO_2 polymorphs was pursued in order to create an efficient heterojunction for sufficient charge separation and increased HER activity under solar light.

Interestingly, the addition of a minimal amount of water (0.5% v/v) during synthesis induced the co-crystallization of anatase TiO_2 along with Cu-FDT, which constituted 34.5% of the crystalline phase in the final composite and at the same calcination temperature and duration (Fig. 3a and Fig. S4a, Table S4). A series of calcination experiments revealed the thermal evolution of the multiphase system, consisting of anatase, rutile, or both, alongside Cu-FDT. When the synthesis reaction product was subjected to calcination at 650 °C/4 h, a portion of the metastable anatase transformed into rutile, resulting in a three-phase system (Cu-FDT, anatase and rutile) with Cu-FDT remaining the main crystalline constituent at 47.2%. Further increase of the calcination temperature at 750 °C, produced a dual-phase system consisting of Cu-FDT and rutile in a 1 : 1 ratio, as a result of the complete transformation of anatase to rutile.[55] Interestingly, higher calcination temperatures (850 °C) induced a profound phase transformation: the Cu-FDT content drastically diminished, concurrent with the crystallization of a copper and sodium titanate perovskite-type phase, identified as $Na(Cu_{2.5}Ti_{0.5})Ti_4O_{12}$ cubic perovskite.[56] This observation suggests that higher calcination temperatures induced a solid-state transition between the freudenbergite and perovskite structures. The crystalline size of the main constituents was calculated through Rietveld Refinement of the powder diffraction pattern for each photocatalyst, with the exemption of Cu-FDT_A sample for which anatase crystallite size could not be safely calculated due to peak overlap with Cu-FDT. The crystallite size of the Cu-FDT phase exhibited a clear upward trend with increasing calcination temperature, increasing from 22.4 nm for the sample containing only anatase and Cu-FDT (Cu-FDT_A) to a maximum of 106.5 nm in the sample calcined at the highest temperature (Fig. S4 and Table S4). This growth can be attributed to Ostwald ripening, a thermally driven process where larger particles grow at the expense of smaller, less stable ones.[57] Notably, the co-crystallization with anatase in the initial Cu-FDT_A sample appeared to supress the growth of Cu-FDT crystallites, constraining them to a size of 10.3 nm. Concurrently, the rutile phase first emerged in the sample Cu-FDT_B with a crystalline size of 73.11 nm. The rutile crystallites also underwent significant growth through Ostwald ripening, ultimately reaching 131.4 nm in sample Cu-FDT_D.

To mitigate the detrimental impact of excess sodium surface Na^+ species, which can act as charge recombination centres and supress photocatalytic activity, a second set of catalysts was

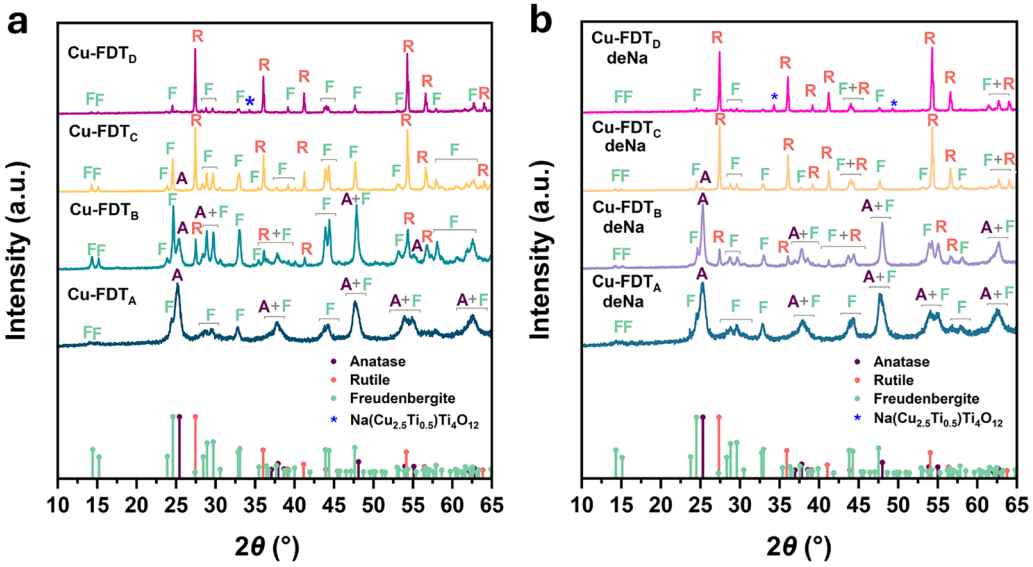

Fig. 3 Effect of calcination temperature on crystalline phase composition of samples (a) Cu-FDT_{A-D} with excess Na^+ and (b) Cu-FDT_{A-D} deNa with stoichiometric Na^+. A: anatase, R: rutile, F: freudenbergite.

prepared following the same calcination protocol, but the staring product of the reaction was subjected to 1 M HCl treatment under ultrasonication to remove surface sodium.[58] This established purification process effectively eliminates alkali-containing impurities, exposing catalytically active sites and potentially enhancing the HER activity of the photocatalysts. After excess sodium removal from the reaction product, the desodiated (deNa) series of photocatalysts followed a similar crystallization pathway to their sodium-rich counterparts, with anatase, rutile and NaCuTi-perovskite nucleating at the same calcination temperatures (Fig. 3 and Table S4). However, the thermal stability of anatase was notably altered. Specifically, it demonstrated significantly enhanced resilience to thermal transformation in the deNa samples, contributing to 39.4% of the crystalline phase in the Cu-FDT$_B$ deNa sample, compared to only 22.5% in the sodium-rich Cu-FDT$_B$ sample calcined at the same temperature. A minor anatase fraction (1.5%) persisted even after calcination at 750 °C (Cu-FDT$_C$). Furthermore, the crystallite size of the Cu-FDT phase, while still following an upward trend with temperature, was consistently smaller across all deNa samples after 1 M HCl treatment (Figure S4, Table S4). Finally, the perovskite phase that formed at 850 °C was present in substantially larger proportion (10.2% *vs.* 3.9%) following sodium removal. This suggests that the elimination of excess surface sodium had a direct impact on the crystallization process and the heterojunctions formed, while it enhanced this specific solid-state transition (Fig. 3 and Table S4).

3.4 Solar-driven photocatalytic H_2 evolution

The photocatalytic hydrogen evolution activities of the synthesized photocatalysts, including bare Cu-FDT, were evaluated under simulated solar light irradiation using TEOA as the sacrificial electron donor. As shown in Fig. 4a and e, bare Cu-FDT exhibited modest HER activity, with an average hydrogen evolution rate of 31.9 $\mu molH_2\ g^{-1}\ h^{-1}$. The low activity is likely attributable to rapid charge-carrier recombination, a common issue in semiconductor photocatalysts lacking a co-catalyst, as well as to the weak reducing character of the Cu-FDT CB position.[59]

In contrast, the Cu-FDT$_A$ sample, which contains a heterojunction between Cu-FDT and anatase, demonstrated a drastically enhanced hydrogen evolution rate at 702.7 $\mu molH_2\ g^{-1}\ h^{-1}$ (Fig. 4b and e). This twenty-two-fold enhancement in the catalytic activity can be attributed to the *in situ* formation of an efficient heterojunction that significantly improves charge separation. The intimate interfacial contact achieved through the concurrent growth and crystallization of Cu-FDT and anatase phases facilitates the creation of an internal electric field, potentially *via* a Type-II or Z-scheme charge transfer mechanism, thereby suppressing recombination and enhancing photocatalytic efficiency. However, HER performance declined to 161.2 $\mu molH_2\ g^{-1}\ h^{-1}$ in the three-phase system (Cu-FDT, anatase and rutile) in sample Cu-FDT$_B$ (Fig. 4b and e). The rate reduction is likely due to the unfavorable electronic band structure of rutile, which may act as a charge recombination center, combined with the decreased anatase content resulting from its phase transition to rutile.

Finally, samples calcined at higher temperatures (Cu-FDT$_C$ and Cu-FDT$_D$) exhibited only trace amounts of H_2. This complete loss of activity can be attributed to the absence of the effective Cu-FDT/anatase heterojunction and the significant increase in nanoparticle size across all remaining phases, a consequence of excessive sintering, which reduces the available surface area and impedes charge transfer to the photocatalyst surface (Fig. 4b and e). It should be noted that the hydrogen evolution *vs.* time plots for all catalytically active samples exhibited a linear trend over the 6-hour irradiation period. This linearity indicates stable photocatalytic activity and suggests no significant photo corrosion or deformation of the catalyst surfaces under the employed reaction conditions.

A dramatic enhancement in photocatalytic hydrogen evolution activity was observed for the deNa catalyst series (Fig. 4c and e). The overall performance trend among the different phases remained consistent with that of the sodium-rich analogues: samples Cu-FDT$_C$ deNa and Cu-FDT$_D$ deNa exhibited minimal activity. However, a remarkable enhancement was recorded for the Cu-FDT/anatase heterojunction in sample Cu-FDT$_A$ deNa, which achieved an average hydrogen evolution of 2297.7 $\mu molH_2\ g^{-1}\ h^{-1}$. This corresponds to more than three-fold increase compared to its sodium-rich counterpart and reveals the true potential of this heterojunction when all catalytic active surface sites are accessible. The mixed-phase sample, Cu-FDT$_B$ deNa, exhibited the second highest activity at 1546.7 $\mu molH_2\ g^{-1}\ h^{-1}$. Although significant, this performance remains limited by the presence of rutile, which, as previously noted, acts as a charge recombination center and thus bottlenecks the overall catalytic efficiency. The pronounced activity increase across the deNa series demonstrates that the removal of excess Na is a pivotal post-synthetic treatment for this system as it eliminates insulating species from the photocatalytic surfaces.

Photoluminescence (PL) spectroscopy recorded under 310 nm excitation was employed to provide insight into the charge carrier dynamics of the individual components and the co-crystallized and desodiated Cu-FDT/anatase (Cu-FDT$_A$ deNa) heterojunction. The pristine TiO_2 sample exhibited the strongest PL emission, while Cu-FDT showed a comparatively lower intensity. Notably, the Cu-FDT$_A$ deNa composite displayed significant quenching of PL compared to its bare constituents. This substantial reduction in emission intensity suggests that co-crystallization promotes intimate interfacial contact and facilitates efficient charge separation across the heterojunction, thereby suppressing radiative recombination pathways.[60]

The better performing photocatalysts of both series containing the Cu-FDT/anatase heterojunction, namely CuFDT$_A$ and Cu-FDT$_A$ deNa, were selected for further investigation and catalytic optimization. To this end, 1 wt% Pt was photodeposited onto each sample to function as a co-catalyst. Pt is widely regarded as the benchmark co-catalyst for HER due to its optimal Fermi level alignment with the CB of many semiconductors, such as anatase-TiO_2, which promotes efficient

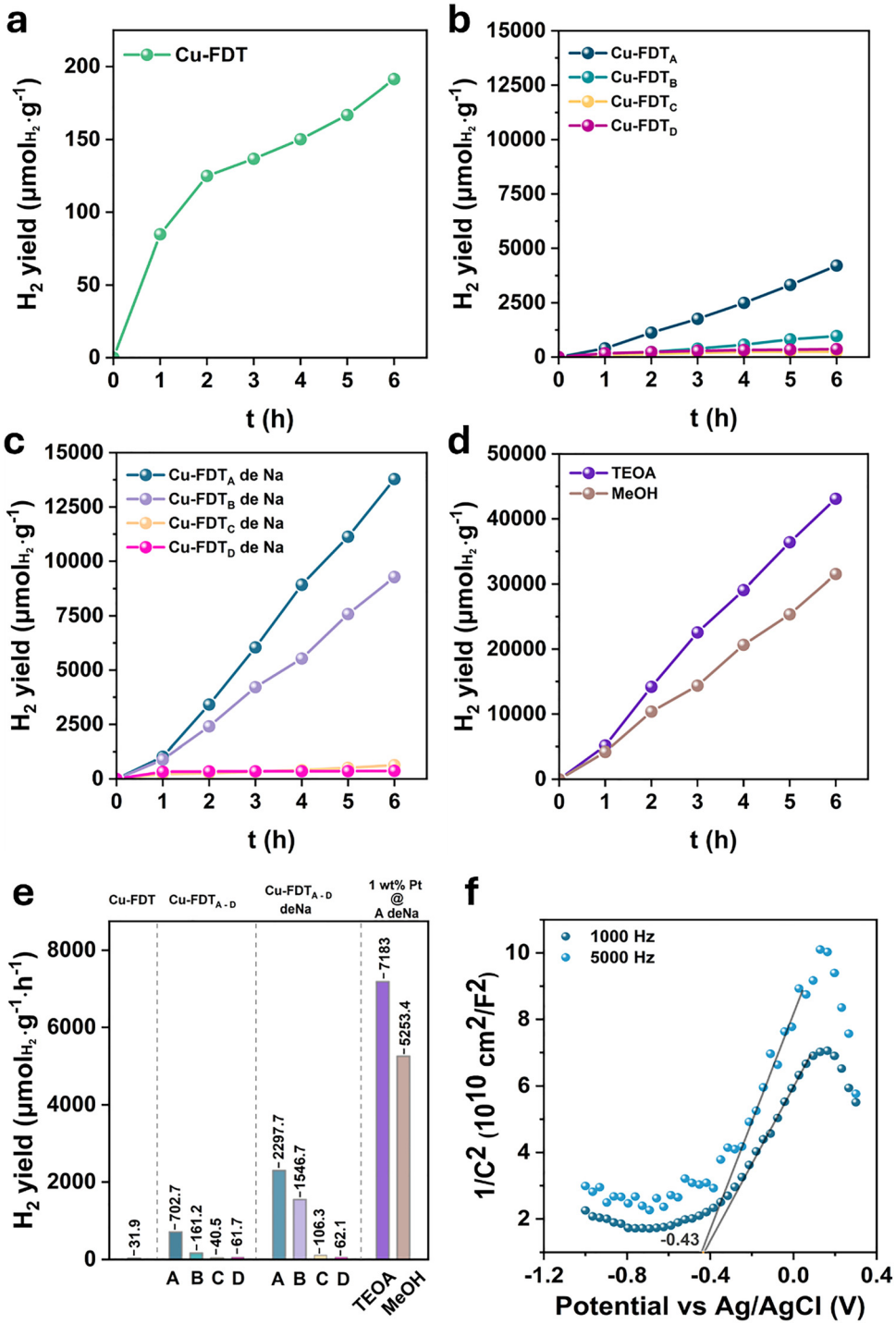

Fig. 4 H_2 evolution over the course of 6 h employing (a) bare Cu-FDT, (b) the sodium-rich heterojunctions in samples Cu-FDT_{A-D}, (c) the desodiated heterojunctions in samples Cu-FDT_{A-D} deNa, (d) TEOA and MeOH as sacrificial donors for the 1 wt% Pt photodeposited Cu-FDT_A deNa photocatalyst.* (e) Average H_2 evolution rates for all systems tested* (f) Mott-Schottky plots for the Cu-FDT_A deNa sample. * Results for 1 wt% Pt@Cu-FDT_A omitted for clarity.

electron extraction and accumulation, coupled with its exceptionally low overpotential for proton reduction.[4] The deposition of 1 wt% Pt as a co-catalyst yielded strikingly divergent outcomes for the two catalysts. The desodiated sample, Cu-FDT_A deNa, exhibited a remarkable enhancement in photocatalytic performance, achieving an average hydrogen evolution rate of 7183 $\mu molH_2\ g^{-1}\ h^{-1}$ in the presence of triethanolamine (TEOA) as a sacrificial electron donor, while upon substitution of TEOA with MeOH the performance dropped to 5253.4 $\mu molH_2\ g^{-1}\ h^{-1}$ (Fig. 4d). This implies that the catalyst

works better under alkaline pH (reaction pH = 11) compared to the use of acidic MeOH as a sacrificial electron donor. The superior activity observed with TEOA indicated that the catalyst operates more efficiently *via* the H_2O reduction pathway than the proton (H^+) reduction one. The alkaline environment supplied by 10% TEOA, facilitated the activation and reduction of water molecules at the catalyst surface. The significantly lower performance in the acidic conditions created by 10% MeOH suggests the limited presence of catalytic sites that favor H^+ adsorption and reduction (Fig. 4d and e). Conversely, Pt deposition to the sodium-rich Cu-FDT$_A$ photocatalyst had an adverse effect, resulting in complete deactivation of the photocatalyst. We propose that in the sodium-rich sample, excess surface Na^+ formed an insulating layer that inhibited the formation of an effective Pt-heterojunction Schottky junction. Instead, the deposited Pt nanoparticles likely functioned as efficient recombination centers for photogenerated charges, thereby quenching all photocatalytic activity. In the desodiated sample, the removal of this passivating layer allowed for optimal interfacial contact between Pt and the semiconductors, facilitating efficient extraction of electrons (e^-) *via* the Schottky junction and their subsequent use for H_2O reduction.[61]

3.5 Photoelectrochemical performance of the Cu-FDT$_A$ and Cu-FDT$_A$ deNa heterojunctions

The interfacial charge transfer dynamics and electrocatalytic activity of the Cu-FDT/anatase heterojunction, in both its as-synthesized (Na^+-rich) and HCl-washed (desodiated) forms, were investigated through transient photocurrent response, EIS and LSV measurements. The transient photocurrent and EIS measurements, conducted in a neutral Na_2SO_4 electrolyte probed the bulk and interfacial charge separation efficiency of the heterojunctions and the individual heterojunction components TiO_2 anatase and Cu-FDT. The Na^+-rich heterojunction (Cu-FDT$_A$) exhibited a stronger instantaneous photocurrent response to solar light (Fig. 5a) than the desodiated counterpart (Cu-FDT$_A$ deNa) while Cu-FDT generated more current than anatase TiO_2 upon simulated solar-light irradiation. Since the

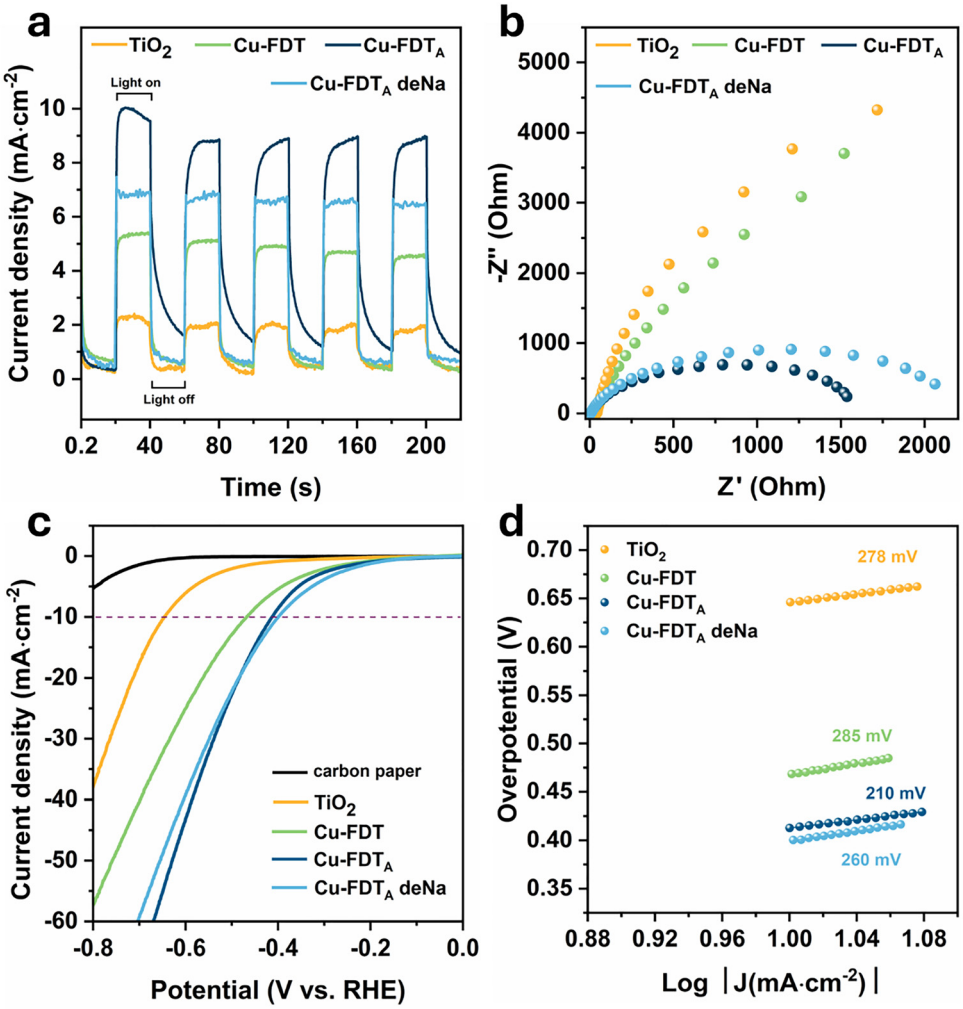

Fig. 5 (a) Photocurrent density response of the synthesized photocatalysts under bias of 0.5 V *vs.* Ag/AgCl, (b) EIS Nyquist plots of the synthesized photocatalysts at 0 V *vs.* Ag/AgCl, (c) LSV HER polarization curves of carbon paper (electrode substrate) and the synthesized photocatalysts recorded in 0.5 M H_2SO_4, (d) corresponding Tafel slopes for HER.

only difference between the two photocatalysts is the existence or lack thereof of surface Na^+ the difference in photogenerated charge carrier is assigned to a Na^+-induced modification of the heterojunction-electrolyte interfacial environment. It has been shown that electrolyte cations, including Na^+, can act as positive surface dipoles, inducing a downward band bending that creates a stronger electric field and drives enhanced charge separation.[62] Such interfacial electrostatic effects rationalize the superior transient photocurrent observed for the Cu-FDT$_A$ heterojunction, where excess Na^+ is strongly adsorbed on the metal-oxide surface, while the reduced photocurrent following desodiation is consistent with partial attenuation of this favorable interfacial field, despite retention of heterojunction-enabled charge separation.

EIS plots further support this conclusion, as Cu-FDT$_A$ exhibits a marginally smaller semicircle radius in the Nyquist plot compared to the optimal for photocatalytic HER, Cu-FDT$_A$ deNa, indicating a lower effective interfacial charge-transfer resistance (Fig. 5b). Both heterojunctions revealed greatly reduced charge-transfer resistance than the bare components Cu-FDT and TiO_2 anatase which indicates the creation of an effective heterojunction.

To further probe the effectiveness of the created heterojunction for HER, LSV was performed in 0.5 M H_2SO_4. Pristine TiO_2 anatase required the highest overpotential to drive HER, followed by Cu-FDT. In contrast, both Cu-FDT$_A$ and Cu-FDT$_A$ deNa heterojunctions exhibited significantly lower overpotentials and similar polarization behavior. Notably the desodiated catalyst (Cu-FDT$_A$ deNa) initiated the HER at a slightly more positive onset potential (Fig. 5c). This trend suggests that the beneficial role of Na^+ observed under illumination does not directly translate into improved electrocatalytic HER activity in acidic media. We attribute this to surface-associated Na^+ ions partially block H^+-accessible sites, thereby hindering proton adsorption and hydrogen evolution relative to the freely accessible surface of the desodiated catalyst Cu-FDT$_A$ deNa.

Tafel analysis, derived from the LSV data, provides complementary insights into the reaction kinetics. Pristine TiO_2 anatase and Cu-FDT exhibit Tafel slopes at 278 and 285 mV dec^{-1}, respectively. The formation of the Cu-FDT/anatase heterojunction substantially improved the kinetics, reducing the Tafel slopes to 210 mV dec^{-1} for Cu-FDT$_A$ and 260 mV dec^{-1} for Cu-FDT$_A$ deNa (Fig. 5d). The superior onset potential of the desodiated sample, despite its higher Tafel slope, indicates that desodiation creates a surface that HER commences more readily, likely due to improved accessibility of active sites and enhanced electronic coupling with the Pt co-catalyst used for photocatalytic HER.

To elucidate the charge transfer mechanism within the Cu-FDT$_A$ deNa heterojunction, electrochemical impedance measurements were conducted to differentiate between a conventional Type-II and a direct Z-scheme pathway. The band edge positions of the anatase reference prepared under identical conditions but in the absence of Cu^{2+}, were derived from the Mott–Schottky (Fig. 5) −0.79 V *vs.* Ag/AgCl, corresponding to a CB minimum at −0.6 V *vs.* NHE. Based on a bandgap of

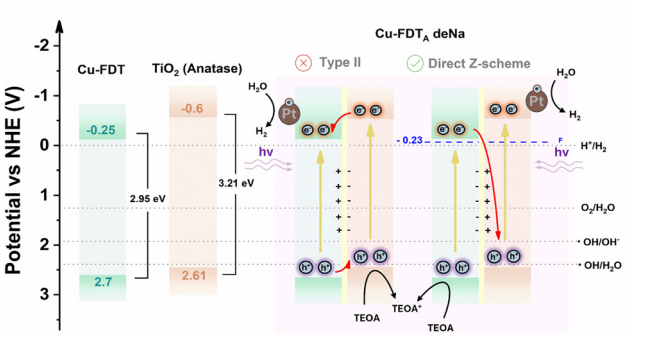

Fig. 6 Proposed Z-scheme charge-transfer for HER and oxidation of TEOA employing the 1 wt% Pt@Cu-FDT$_A$ deNa photocatalyst.

3.21 eV, its VB maximum was calculated to reside at +2.61 V *vs.* NHE (Fig. S6 and S7), consistent with literature values for anatase TiO_2.[63] In contrast, the Cu-FDT$_A$ deNa heterojunction exhibited a composite flat-band potential that was shifted anodically to −0.43 V *vs.* Ag/AgCl. This positive displacement of the apparent flat-band potential relative to the conduction bands of the constituent semiconductors suggests the formation of an internal electric field across the interface and indicated a modified interfacial electronic structure.[64] Such anodic shift can be interpreted as supporting a direct Z-scheme configuration, in which selective charge recombination occurs between e^- in the CB of Cu-FDT and the h^+ in the VB of anatase, rather than the delocalized charge redistribution typical of a Type-II junction (Fig. 6).[65] In this configuration, photoexcitation of both semiconductors with solar-light promotes charge carrier separation, preserving the most energetic species, that are the h^+ in the highly oxidative VB of Cu-FDT and the e^- in the CB of anatase. These remaining carriers subsequently participate in surface redox reactions, where the h^+ oxidize TEOA and the e^- are transferred to the Pt co-catalyst to promote HER. Although we cannot completely rule out the existence of a Type II heterojunction between these materials, the observed anodic shift, when considered together with the relative band edge positions and the known electronic structure of both phases, provides compelling electrochemical evidence consistent with a direct Z-scheme mechanism rather than a conventional Type-II heterojunction (Fig. 6).[66,67]

3.6 Solar driven photooxidation of 5-(hydroxymethyl)furfural (5-HMF)

To evaluate the potential for a concurrent dual-function process coupling H_2 evolution with5-HMF oxidation, initial experiments were carried out using the top performing HER photocatalysts, Cu-FDT$_A$ and Cu-FDT$_A$ deNa along with their Pt loaded counterparts, with 5-HMF serving as the sole electron donor (Fig. S8). The results confirmed that 5-HMF can effectively act as an electron donor for these systems. The maximum H_2 evolution rate reached 297.4 μmolH_2 g^{-1} h^{-1} for 1 wt% Pt@Cu-FDT$_A$. Notably, while Pt photodeposition enhanced the HER activity of the sodium-rich photocatalyst (Cu-FDT$_A$), its

performance was comparable to the unloaded desodiated catalyst (Cu-FDT$_A$ deNa). Interestingly, Pt loading on Cu-FDT$_A$ deNa resulted in complete catalyst deactivation. This suggests that Na removal significantly alters the catalyst surface, leading to a stronger Pt–support interaction that blocks active sites required for 5-HMF adsorption and oxidation, thereby suppressing the coupled redox process.[68,69]

To evaluate the oxidation performance and selectivity of the synthesized Cu-FDT/anatase heterojunctions which showed the highest activity for solar driven HER as well as that of the 1 wt% Pt samples, two different sets of experiments were conducted. First, a screening test was performed using 10 mM 5-HMF solutions and a 12 h irradiation period in the presence of 0.2 mg ml^{-1} of each catalyst. Subsequently, the top-performing catalyst from the screening was selected and a second series of experiments designed to assess the influence of solvent composition and O_2 availability on activity and selectivity. Specifically, the H_2O content was varied from 100% to 20% in MeCN and the atmosphere was altered from inert (Ar saturated) to O_2-saturated, under a shorter irradiation time of 6 hours. This strategy aimed to correlate water content and oxygen-dependent reactive oxygen species (ROS) generation with catalytic activity. The conversion efficiency was primarily monitored *via* UV-Vis spectroscopy, based on the depletion of the characteristic $\pi \rightarrow \pi^*$ transition absorption band of the 5-HMF furanic ring at 284 nm, while the liquid-phase products were detected *via* HPLC. Fig. 7a and b reveals the intrinsic photocatalytic oxidation ability of the selected photocatalysts toward 5-HMF. The highest performance was achieved by the Cu-FDT$_A$ deNa catalyst, which attained 89.7% degradation of 5-HMF over 12 hours of irradiation, corresponding to a degradation rate of 3.74 mmol$_{5\text{-HMF}}$ g^{-1} h^{-1}. Notably, the addition of 1 wt% Pt although beneficial for HER due to its role as a co-catalyst for electron extraction and recombination suppression did not enhance the oxidative performance of either the sodium-rich or the desodiated

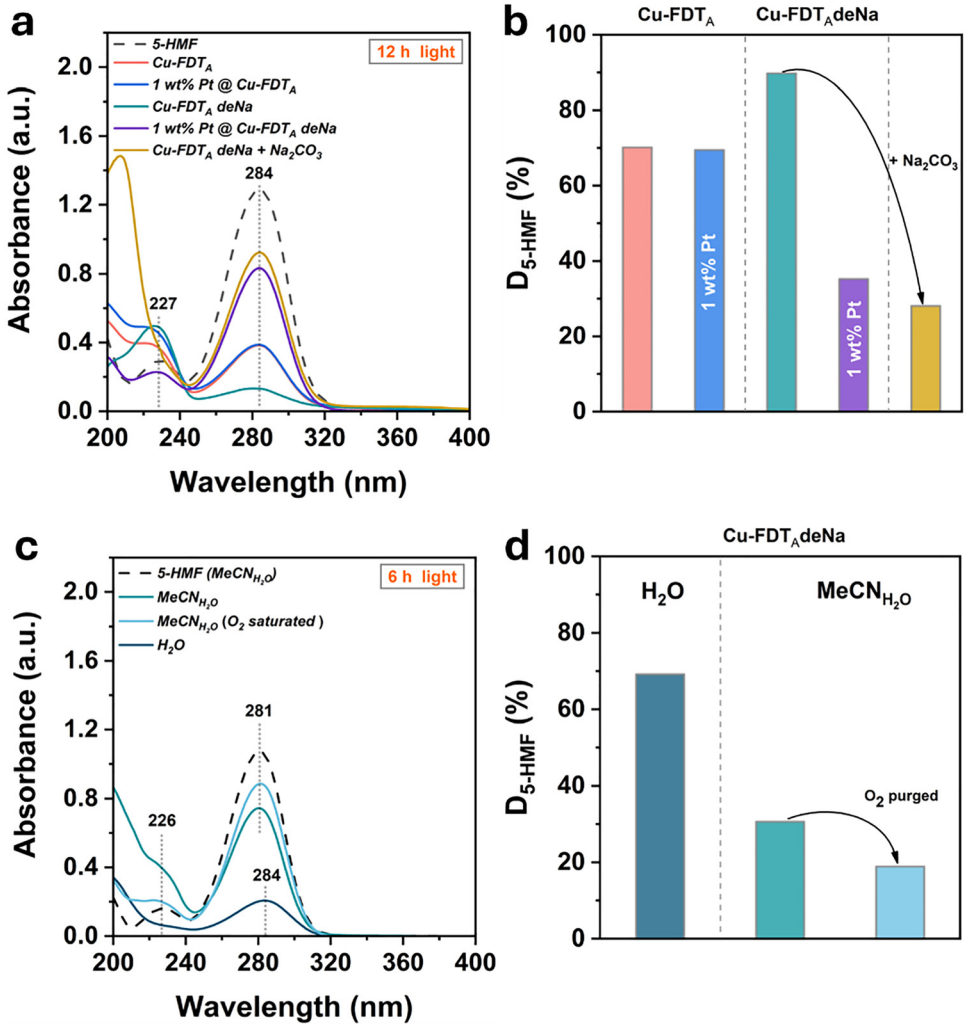

Fig. 7 (a) UV-Vis screening of the synthesized catalysts with 10 mM 5-HMF as substrate and scavenging with Na_2CO_3 for a reaction duration of 12 h. (b) Degradation percentage of 5-HMF using selected photocatalysts for a reaction duration of 12 h. (c) UV-Vis spectra of the reaction solutions employing Cu-FDT$_A$ deNa with different reaction conditions and reaction duration of 6 h. (d) Degradation percentage of 5-HMF in H_2O and MeCN 80% using 5 mg of Cu-FDT$_A$ deNa, 10 mM 5-HMF and 6 h of light irradiation.

catalyst. This suggests that the improved charge separation facilitated by Pt does not directly translate into a higher concentration of reactive h^+ available for 5-HMF oxidation. We propose that Pt nanoparticles may preferentially occupy surface sites crucial for the adsorption of 5-HMF, a critical initial step in its oxidation pathway. As a result, the reaction kinetics may become limited by substrate adsorption rather than charge carrier availability. Despite this, the Na-rich catalysts (Cu-FDTA and 1 wt% Pt@Cu-FDT$_A$) demonstrated significant activity, achieving 69.7% and 70% degradation, respectively. This result indicates a favorable interaction between surface sodium species and 5-HMF, potentially Brønsted-basic in character, through Na–O-bonding, that enhances the binding of 5-HMF through its aldehyde group and facilitates subsequent oxidation.[70–72] HPLC analysis revealed that photocatalytic oxidation of 5-HMF over the heterojunction catalysts resulted primarily in complete mineralization, as it can be concluded by the rise in the absorption at 226 - 227 nm arising from formic acid (FA) (Figure S9 and Fig. 7a). Only trace intermediates, HMFCA and DFF, were detected with the sodium-rich Cu-FDT/anatase heterojunctions and with the more active oxidative catalyst, Cu-FDTA deNa. This high degree of mineralization is attributed to the strong adsorption of 5-HMF onto the catalyst surface, coupled with the high oxidative potential of valence band-h^+ at Cu-FDT, which enables deep oxidation (Fig. 6).[73,74] To probe the role of reactive species, Na_2CO_3, a known h^+ scavenger was introduced, resulting in a sharp reduction of the 5-HMF degradation rate to 28% using Cu-FDT$_A$ deNa. This strong inhibition clearly confirms that photogenerated h^+ are the dominant oxidative species driving 5-HMF oxidation (Fig. 7a and b).[75] Furthermore, no shift of the absorption peak of 5-HMF at 384 nm was observed, indicating a persistent hole-mediated oxidation toward deep oxidation products rather than through a selective pathway.[76]

The roles of solvent and O_2 in the photocatalytic reaction, were assessed by further testing the top-performing Cu-FDT$_A$ deNa heterojunction under controlled conditions (Fig. 7c and d). In pure aqueous medium and under Ar-saturated atmosphere, 69% degradation was achieved after 6 hours of irradiation, owing to the higher catalyst loading (Fig. 7d). The high activity observed in O_2-deficient atmosphere supports the high participation of h^+ in the oxidation of 5-HMF, alongside the pathway involving molecular O_2-derived ROS such as the superoxide radical ($^{\bullet}O_2^-$), hydrogen peroxide (H_2O_2), hydroxyl radicals ($^{\bullet}OH$) or singlet oxygen ($^1O_2$). The importance of the aqueous environment was further underscored by experiments performed in a mixed solvent system ($MeCN_{H_2O}$, 80% v/v MeCN). A sharp drop in activity, resulting in only 31% degradation was observed (Fig. 7d). This drastic reduction can be attributed to two main factors, namely, the decreased concentration of H_2O which contributes to ROS generation and the competitive adsorption of MeCN onto the catalyst surface, which blocks active sites and hinders 5-HMF adsorption.[73] Performing the reaction in O_2-rich atmosphere further quenched the reaction rate. This result suggests that O_2 competes with 5-HMF for photogenerated h^+, rather than acting as an e^- scavenger, thereby enhancing the oxidative performance of the photocatalyst.[77]

Conclusions

Overall, the successful synthesis of a Cu-substituted freudenbergite was demonstrated for the first time, using a co-precipitation method. Comprehensive characterization-using PXRD, XPS, STEM-EDS and HR-TEM-confirmed the formation of the material and the presence of Ti^{3+} species for charge compensation. The band gap was estimated at 2.95 eV from UV-DRS using the Kubelka–Munk method, while Mott–Schottky analysis revealed a Fermi band located at −0.25 V *vs.* NHE (pH = 7). By adding a small amount of H_2O to the precursor solution prior to precipitation, we achieved the *in situ* fabrication of heterojunctions between Cu-FDT and TiO_2. The phase composition of TiO_2 (anatase, rutile) was controllably tuned by varying calcination temperature. The presence of excess surface Na^+ was found to influence the stability and thermodynamic phase transitions of TiO_2 as well as the stability of Cu-FDT. The photocatalytic performance of the heterojunctions was evaluated for solar light driven HER using TEOA as a sacrificial electron donor. The most active catalyst was the desodiated Cu-FDT/anatase heterojunction (Cu-FDT$_A$ deNa), which, when loaded with 1 wt% Pt, achieved a remarkable rate of 7183 $\mu molH_2\ g^{-1}\ h^{-1}$. Photocatalytic experiments, transient photocurrent, EIS, and HER polarization with Tafel analysis collectively elucidated the dual-phase influence of the excess surface Na^+ on the HER activity of the Cu-FDT/anatase heterojunction. Pl quenching and Mott–Schottky analysis indicated a direct Z-scheme charge transfer process, enabling utilization of the highly reductive CB of anatase TiO_2 and the highly oxidative VB of Cu-FDT. Furthermore, the Cu-FDTA deNa catalyst demonstrated excellent oxidative capability, achieving 89.7% mineralization of 5-HMF after 12 hours of simulated solar-light irradiation, owing to the oxidative power of photogenerated h^+ on the VB of the Cu-FDT component. These findings establish Cu-FDT-based heterojunctions as promising photocatalysts for simultaneous hydrogen production and biomass-derived compound oxidation, opening new directions for solar-driven energy and chemical conversion.

Author contributions

P. T.: writing – original draft, conceptualization, investigation, formal analysis, data curation, and visualization. E. S.: investigation. L. K.: data curation. O. M.: investigation. N. B.: resources, C. A. M.: project administration, funding acquisition, supervision, resources, writing – review & editing.

Conflicts of interest

There are no conflicts to declare.

Data availability

The data supporting this article are provided in supplementary information (SI). The SI includes Rietveld refinement data (fitted pattern, atomic coordinates, fit statistics and cell parameters); TEM and HR-TEM images and particle distribution of Cu-FDT; elemental composition obtained by EDS and XPS. Additional XPS and XRD analyses, phase identification, and crystallite size determination are included, along with PL data, as well as Mott–Schottky and Kubelka–Munk plots of TiO_2 anatase. The SI also contains additional H_2-evolution experiments using 5-HMF as the electron donor, as well as the HPLC chromatographs for the determination of 5-HMF oxidation products. See DOI: https://doi.org/10.1039/d5ya00313j.

Acknowledgements

The publication of this article in OA mode was financially supported by HEAL-Link and co-funded by the Special Research Account of NKUA (No. 19712). The authors would like to acknowledge Dr Labrini Sygellou for conducting the X-Ray photoelectron spectroscopy (XPS) measurements at the Surface Science Characterization Laboratory in the Institute of Chemical Engineering Sciences, FORTH-ICEHT. All powder diffraction data were collected in the National and Kapodistrian University of Athens X-Ray Diffraction Core Facility. The assistance of MSc Maria Kourmousi with the electrochemical impedance measurements is also gratefully acknowledged.

References

1 J. D. Burrington, *ACS Omega*, 2024, **9**, 25841–25858.
2 M. Yue, H. Lambert, E. Pahon, R. Roche, S. Jemei and D. Hissel, *Renewable Sustainable Energy Rev.*, 2021, **146**, 111180.
3 A. D. G. Kafadi, H. Y. Hafeez, J. Mohammed, C. E. Ndikilar, A. B. Suleiman, A. T. Isa and F. K. Alharbi, *Eur. J. Inorg. Chem.*, 2025, e202500191.
4 K. Maeda and K. Domen, *J. Phys. Chem. Lett.*, 2010, **1**, 2655–2661.
5 M. Mohsin, I. A. Bhatti, M. Zeshan, M. Yousaf and M. Iqbal, Elsevier B.V., 2023, preprint, DOI: 10.1016/j.flatc.2023.100547.
6 P. Tzevelekidis, M. Theodosiou, A. Papadopoulou, E. Sakellis, N. Boukos, A. K. Bikogiannakis, G. Kyriakou, E. K. Efthimiadou and C. A. Mitsopoulou, *Heliyon*, 2024, **10**, e35634.
7 S. Ahmetović, Z. Vasiljević, J. B. Krstić, M. Finšgar, D. Solonenko, D. Bartolić, N. B. Tadić, G. Miskovic, N. Cvijetićanin and M. V. Nikolic, *Surf. Interfaces*, 2024, **49**, 104434.
8 A. Chauhan, S. Agnihotri and M. Vasundhara, *Environ. Sci. Pollut. Res.*, 2024, **31**, 47991–48013.
9 L. Yang, C. Wang, Y. Li, W. Ge, L. Tang, J. Shen, Y. Zhu and C. Li, *Adv. Funct. Mater.*, 2024, **34**, 2401094.
10 L. T. Pérez-Poyatos, S. Morales-Torres, L. M. Pastrana-Martínez and F. J. Maldonado-Hódar, *Catal. Today*, 2025, **446**, 115115.
11 L. Li, Y. Wang, Y. Ruan, T. Xu, S. Wu and W. Lu, *Appl. Surf. Sci.*, 2024, **672**, 160771.
12 L. Sui, W. Chen, X. Long, J. Liao, S. Wang and X. Wei, *Int. J. Hydrogen Energy*, 2024, **55**, 855–863.
13 Z. Jiang, Z. Y. Zhang, W. Shangguan, M. A. Isaacs, L. J. Durndell, C. M. A. Parlett and A. F. Lee, *Catal. Sci. Technol.*, 2016, **6**, 81–88.
14 P. Tzevelekidis, E. Sakellis, N. Boukos, A. K. Bikogiannakis, G. Kyriakou, J. Praxmair, G. A. Zickler, S. Pokrant and C. A. Mitsopoulou, *J. Mater. Chem. A*, 2025, **13**, 39859–39876.
15 C. Hu, Y. K. Jhao, Y. T. Chang, L. H. Kao, K. S. Chuang, J. H. Huang and A. Wibowo, *J. Alloys Compd.*, 2025, **1032**, 181104.
16 Y. Liu, X. Zheng, Y. Yang, J. Li, W. Liu, Y. Shen and X. Tian, *ChemCatChem*, 2022, **14**, e202101439.
17 B. Zhang, F. Liu, B. Sun, T. Gao and G. Zhou, *Chin. J. Catal.*, 2024, **59**, 334–345.
18 B. H. Xiao, C. Huo, J. Y. Chen, Y. G. Xiao, S. S. Cao and Z. Q. Liu, *Chem. Sci.*, 2025, **16**, 4876–4883.
19 D. R. Eddy, M. D. Permana, L. K. Sakti, G. A. N. Sheha, G. A. N. Solihudin, S. Hidayat, T. Takei, N. Kumada and I. Rahayu, *Nanomaterials*, 2023, **13**, 704.
20 S. N. Kulkarni, R. Ragesh Nath, K. Alkanad, A. Amasegowda, S. C. Ke and N. K. Lokanath, *J. Alloys Compd.*, 2025, **1016**, 178876.
21 D. Li, R. Li, D. Zhou, X. Qin and W. Yan, *Fuel*, 2025, **388**, 134237.
22 D. P. Opra, V. V. Zheleznov, S. L. Sinebryukhov, A. A. Sokolov, A. M. Ziatdinov, A. B. Podgorbunsky, A. V. Gerasimenko, A. Y. Ustinov, V. G. Kuryavy, D. A. Saritsky, A. I. Neumoin, N. I. Zaytsev, N. V. Polyakova and S. V. Gnedenkov, *J. Power Sources*, 2024, **600**, 234230.
23 C. Wu, Z. G. Wu, X. Zhang, R. Rajagopalan, B. Zhong, W. Xiang, M. Chen, H. Li, T. Chen, E. Wang, Z. Yang and X. Guo, *ACS Appl. Mater. Interfaces*, 2017, **9**, 43596–43602.
24 P. Yang, L. Xu, Y. Tao, W. Wang, X. Wu and D. Zhang, *J. Electroanal. Chem.*, 2024, **954**, 118051.
25 T. Ishiguro, K. Tanaka, F. Marumo, M. G. M. U. Ismail, S. Hirano and S. Sōmiya, *Acta Crystallogr., B. Struct. Crystallogr. Cryst. Chem.*, 1978, **34**, 255–256.
26 Z. Q. Guo, N. X. Miao, J. P. Zhou, Y. X. Lei, Q. U. Hassan and M. M. Zhou, *J. Mater. Chem. A*, 2017, **5**, 17589–17600.
27 G. Bruhn, S. Beutel, G. Pfaff and B. Albert, *J. Alloys Compd.*, 2015, **644**, 783–787.
28 E. Morgado, B. A. Marinkovic, P. M. Jardim, M. A. S. De Abreu, M. D. G. C. Rocha and P. Bargiela, *Mater. Chem. Phys.*, 2011, **126**, 118–127.
29 Q. W. Chen, Z. Q. Guo and J. P. Zhou, *Appl. Surf. Sci.*, 2024, **648**, 158689.
30 E. Morgado, B. A. Marinkovic, P. M. Jardim, M. A. S. De Abreu, M. D. G. C. Rocha and P. Bargiela, *Mater. Chem. Phys.*, 2011, **126**, 118–127.
31 R. G. Ciocarlan, E. M. Seftel, R. Gavrila, M. Suchea, M. Batuk, M. Mertens, J. Hadermann and P. Cool, *J. Alloys Compd.*, 2020, **820**, 153403.

32 H. Tang, R. Yang and W. Gao, *Phys. B*, 2018, **534**, 120–124.
33 P. Umek, M. Pregelj, A. Gloter, P. Cevc, Z. Jaglicic, M. Čeh, U. Pirnat and D. Arčon, *J. Phys. Chem. C*, 2008, **112**, 15311–15319.
34 A. Belman, A. Jayarama, A. S. Rao, S. S. Nagarkar, A. Dutta, S. P. Duttagupta, S. S. Prabhu and R. Pinto, *Int. J. Hydrogen Energy*, 2024, **81**, 1442–1466.
35 M. Wang, H. Zhou and F. Wang, *Joule*, 2024, **8**, 604–621.
36 X. Su, T. Xiao, Q. Gong, H. Cheng and F. Zhao, *Green Chem.*, 2025, **27**, 9846–9861.
37 X. Bao, M. Liu, Z. Wang, D. Dai, P. Wang, H. Cheng, Y. Liu, Z. Zheng, Y. Dai and B. Huang, *ACS Catal.*, 2022, **12**, 1919–1929.
38 W. Zhang, Q. Li and H. Xia, *Appl. Surf. Sci.*, 2023, **613**, 156036.
39 Z. Luo, Y. Zhu, Y. luo, G. Ren, Y. Wang and H. Tang, *Acta Phys.-Chim. Sin.*, 2025, 100166.
40 F. Kamatsos, M. Drosou and C. A. Mitsopoulou, *Int. J. Hydrogen Energy*, 2021, **46**, 19705–19716.
41 L. Shi, K. Chen, T. Huang, Y. Zhang, Z. Wang and Q. Zhang, *Ceram. Int.*, 2024, **50**, 23937–23944.
42 M. Zhang, M. Liu, K. Han, Y. Liang, X. Zhao, L. Han, J. Wang, S. Wang and Y. Li, *Molecules*, 2024, **29**, 5385.
43 R. G. Ciocarlan, E. M. Seftel, R. Gavrila, M. Suchea, M. Batuk, M. Mertens, J. Hadermann and P. Cool, *J. Alloys Compd.*, 2020, **820**, 153403.
44 M. Hodos, E. Horváth, H. Haspel, Á. Kukovecz, Z. Kónya and I. Kiricsi, *Chem. Phys. Lett.*, 2004, **399**, 512–515.
45 V. D. Chinh, A. Broggi, L. Di Palma, M. Scarsella, G. Speranza, G. Vilardi and P. N. Thang, *J. Electron. Mater.*, 2018, **47**, 2215–2224.
46 H. Dai, W. Xu, K. Yu and W. Wei, *Chin. Chem. Lett.*, 2019, **30**, 517–520.
47 M. C. Biesinger, *Surf. Interface Anal.*, 2017, **49**, 1325–1334.
48 S. Tsatsos and G. Kyriakou, *J. Phys. Chem. C*, 2023, **127**, 6337–6346.
49 Y. Bourlier, M. Bouttemy, O. Patard, P. Gamarra, S. Piotrowicz, J. Vigneron, R. Aubry, S. Delage and A. Etcheberry, *ECS J. Solid State Sci. Technol.*, 2018, **7**, P329–P338.
50 L. H. C. Andrade, S. M. Lima, A. Novatski, A. M. Neto, A. C. Bento, M. L. Baesso, F. C. G. Gandra, Y. Guyot and G. Boulon, *Phys. Rev. B: Condens. Matter Mater. Phys.*, 2008, **78**, 224202.
51 M. D. Roy, T. P. Gompa, S. M. Greer, N. Jiang, L. S. Nassar, A. Steiner, J. Bacsa, B. W. Stein and H. S. La Pierre, *J. Am. Chem. Soc.*, 2024, **146**, 5560.
52 Y. Chen, X. Feng, Y. Liu, X. Guan, C. Burda and L. Guo, *ACS Energy Lett.*, 2020, **5**, 844–866.
53 Z. Zhang and J. T. Yates, *Chem. Rev.*, 2012, **112**, 5520–5551.
54 A. J. Bard and L. R. Faulkner, *Electrochemical methods: fundamentals and applications*, John Wiley & Sons, Inc., 2001.
55 B. N. Cardoso, E. C. Kohlrausch, M. T. Laranjo, E. V. Benvenutti, N. M. Balzaretti, L. T. Arenas, M. J. L. Santos and T. M. H. Costa, *Int. J. Photoenergy*, 2019, **2019**, 7183978.
56 M. Avdeev and V. B. Nalbandyan, *Inorg. Chem.*, 2006, **45**, 2217–2220.
57 D. D. Eberl and J. Srodon, *Am. Mineral.*, 1988, **73**, 1335–1345.
58 G. C. C. Viana, D. L. S. Maia, D. A. S. Rodrigues, L. F. S. Ribeiro, I. O. Mazali, F. Rodrigues-Silva, M. C. V. M. Starling, T. A. Neves and C. C. Amorim, *Journal of Water Process Engineering*, 2025, **77**, 108441.
59 Q. Li, C. Wang, H. Yao, C. He, C. Guo and Y. Hu, *Coord. Chem. Rev.*, 2025, **535**, 216652.
60 L. Xie, P. Wu, Q. Lei, C. Xu, W. Huang, X. Chen, K. Yang and H. He, *Catalysts*, 2023, **13**, 583.
61 T. Ano, F. Kishimoto, S. Tsubaki, Y. H. Lu, J. N. Hohman, M. M. Maitani, M. Salmeron and Y. Wada, *J. Phys. Chem. C*, 2021, **125**, 13984–13989.
62 A. Molinari, A. Maldotti and R. Amadelli, *Catal. Today*, 2017, **281**, 71–77.
63 V. Pfeifer, P. Erhart, S. Li, K. Rachut, J. Morasch, J. Brötz, P. Reckers, T. Mayer, S. Rühle, A. Zaban, I. Mora Seró, J. Bisquert, W. Jaegermann and A. Klein, *J. Phys. Chem. Lett.*, 2013, **4**, 4182–4187.
64 X. Li, J. Yu, J. Low, Y. Fang, J. Xiao and X. Chen, *J. Mater. Chem. A*, 2015, **3**, 2485–2534.
65 W. Zhao, W. Ma, C. Chen, J. Zhao and Z. Shuai, *J. Am. Chem. Soc.*, 2004, **126**, 4782–4783.
66 B. Liu, X. Liu, J. Liu, C. Feng, Z. Li, C. Li, Y. Gong, L. Pan, S. Xu and C. Q. Sun, *Appl. Catal. B*, 2018, **226**, 234–241.
67 L. Ma, S. Liu, J. Xu, N. Zhao, S. Li, W. Jiang, Z. Pan, B. Yang, Y. Liu and B. Lai, *J. Environ. Manage.*, 2025, **391**, 126674.
68 P. Vernoux, A. Y. Leinekugel-Le-Cocq and F. Gaillard, *J. Catal.*, 2003, **219**, 247–257.
69 I. V. Yentekakis, G. Moggridge, C. G. Vayenas and R. M. Lambert, *J. Catal.*, 1994, **146**, 292–305.
70 L. Chico-Mesa, A. Rodes, R. M. Arán-Ais and E. Herrero, *Nat. Commun.*, 2025, **16**, 1–11.
71 S. Li, M. Dong, J. Yang, X. Cheng, X. Shen, S. Liu, Z. Q. Wang, X. Q. Gong, H. Liu and B. Han, *Nat. Commun.*, 2021, **12**, 584.
72 A. Ulyankina, S. Mitchenko and N. Smirnova, *Processes*, 2020, **8**, 647.
73 U. I. Gaya and A. H. Abdullah, *J. Photochem. Photobiol., C*, 2008, **9**, 1–12.
74 S. Yurdakal, B. S. Tek, O. Alagöz, V. Augugliaro, V. Loddo, G. Palmisano and L. Palmisano, *ACS Sustainable Chem. Eng.*, 2013, **1**, 456–461.
75 B. Zhou, J. Song, Z. Zhang, Z. Jiang, P. Zhang and B. Han, *Green Chem.*, 2017, **19**, 1075–1081.
76 N. Cascelli, V. Gotor-Fernández, I. Lavandera, G. Sannia and V. Lettera, *Int. J. Mol. Sci.*, 2023, **24**, 16861.
77 J. B. G. Filho, I. F. Silva, M. Alafandi and J. Rabeah, *Molecules*, 2023, **28**, 8077.